

Effect of Containership Bulkhead Numbers and Thickness on Hydrodynamic Pressure Using Boundary Element Method

Eferebo Sylvanus Ibietela¹, Olusegun Samuel Dare^{2*}

¹CEO, Somatrix Marine Limited, Abuja, Nigeria

²Lecturer I, Department of Marine Engineering, Nigeria Maritime University, Okerenkoko, Delta State, Nigeria

Abstract: This study employs the Boundary Element Method (BEM) to analyze the impact of bulkhead number and plating thickness on hydrodynamic pressure distribution across a vessel's hull. The objective is to quantify and visualize the effects of structural variations on pressure dynamics. BEM simulations revealed that vessels with 20 bulkheads and 25mm plating exhibit localized pressure concentrations reaching 180 N/mm², indicating high rigidity. Conversely, vessels with 10 bulkheads and 20mm plating show a more uniform distribution with critical pressures around 160 N/mm², suggesting increased flexibility. Configurations with 5 bulkheads and 25mm plating also displayed pressures near 180 N/mm², but with a more dispersed pattern. The BEM analysis showcased the compartmentalization of pressure, with increased bulkheads creating distinct pressure zones. These findings highlight a critical trade-off between rigidity and flexibility. Vessels with higher bulkhead counts and thicker plating sustain greater localized pressures, while those with fewer bulkheads distribute pressure more evenly. The BEM effectively mapped pressure gradients, providing crucial insights for structural design and cargo management, ultimately enhancing vessel safety.

Keywords: Boundary Element Method (BEM), Hydrodynamic Pressure, Vessel Hull, Bulkhead Number, Bulkhead Plate Thickness, Structural Rigidity.

1. Introduction

Containerships play a pivotal role in global trade, serving as essential vehicles for the transportation of goods across vast oceans. The structural integrity and hydrodynamic performance of these vessels are critical to ensuring their operational safety and efficiency. One of the key structural features of a containership is its system of bulkheads, which are transverse or longitudinal walls dividing the ship into compartments. Bulkheads provide additional rigidity, limit the spread of damage in case of flooding, and contribute to the vessel's overall structural resilience [1]. However, the design and configuration of bulkheads—particularly their number and thickness—can significantly influence the hydrodynamic pressure distribution experienced by the ship's hull during operation [2].

Hydrodynamic pressure, resulting from the interaction of the vessel with surrounding water and waves, is a critical parameter

in ship design. Excessive or uneven pressure can lead to structural fatigue, excessive deformation, and, in extreme cases, catastrophic failure [3]. Computational techniques such as the Boundary Element Method (BEM) offer a robust and efficient approach to analyzing the hydrodynamic response of containerships under various conditions. The BEM enables precise modeling of the fluid-structure interaction, providing insights into how different design parameters impact hydrodynamic pressures and subsequent structural stresses [4].

While previous studies have investigated factors such as hull form, wave frequency, and vessel speed on hydrodynamic response, the specific role of bulkhead design parameters remains relatively underexplored. Bulkhead configuration not only affects the vessel's structural rigidity but also influences its dynamic response in waves [5]. Variations in the number of bulkheads and their thickness alter the distribution of stiffness along the hull, which in turn impacts the interaction between the vessel and the surrounding fluid.

This study investigates the effect of bulkhead number and thickness on the hydrodynamic pressure distribution in containerships using the Boundary Element Method. The primary objective is to establish a detailed understanding of how these structural parameters influence hydrodynamic performance, contributing to more optimized vessel designs. The research focuses on analyzing the hydrodynamic pressure distribution for varying bulkhead configurations, with particular attention to its implications for safety, structural efficiency, and economic performance of containerships [6]. By bridging the gap between structural design and hydrodynamic analysis, this work aims to provide valuable insights into the interplay between bulkhead design and hydrodynamic forces, offering a foundation for future design improvements and enhancing the reliability of containerships in challenging maritime environments.

2. Literature Review

The efficient and safe operation of containerships, vital for global trade, depends significantly on a deep understanding of their structural behavior under various loading conditions.

*Corresponding author: olusegunsamuel252@yahoo.com

Hydrodynamic pressure exerted on internal bulkheads, particularly during wave-induced motions and sloshing, is a critical factor influencing structural integrity [1]. This pressure can induce substantial stresses, potentially leading to structural failure if not adequately addressed. This review explores the current knowledge regarding the effect of bulkhead number and thickness on hydrodynamic pressure in containerships, highlighting key research and identifying areas for further study.

Early investigations into hydrodynamic pressure in ship structures primarily utilized simplified analytical models and scaled model experiments [7]. These provided valuable insights into general pressure distribution behavior under static and dynamic loads. However, the complexity of containership hull forms and the non-linear nature of wave-induced phenomena often limited the accuracy of these simplified methods. With increasing computational power, numerical methods, especially potential flow and Computational Fluid Dynamics (CFD), have become increasingly prevalent for analyzing hydrodynamic pressures [8].

The number of bulkheads within a containership significantly affects the overall structural response. More bulkheads can enhance longitudinal strength and stiffness, reducing hull girder bending moments and deflections. However, each bulkhead also introduces structural discontinuities, which can act as stress concentration points under hydrodynamic loading. Furthermore, bulkhead spacing and arrangement influence internal tank volumes and free surface areas, affecting sloshing pressure magnitude and distribution. Research has shown that optimizing bulkhead placement is crucial to minimize hydrodynamic loads while maintaining structural integrity and cargo capacity [9].

Bulkhead thickness is another critical parameter influencing structural resistance to hydrodynamic pressure. Thicker bulkheads offer greater strength and stiffness, reducing the likelihood of yielding or buckling under pressure loads. However, increasing thickness adds weight, potentially reducing cargo capacity and increasing fuel consumption. Therefore, determining optimal thickness involves a trade-off between structural strength and operational efficiency. Studies have investigated the relationship between thickness and hydrodynamic pressure, considering various loading scenarios, including wave-induced motions, sloshing, and slamming [11]; [12].

Accurate prediction of hydrodynamic pressure on bulkheads requires sophisticated numerical techniques. Potential flow methods, while computationally efficient, often struggle to capture complex free surface effects and viscous phenomena associated with wave breaking and sloshing. CFD methods, conversely, offer higher fidelity by solving the Navier-Stokes equations but are computationally more demanding. Recent research has focused on developing and validating CFD models for simulating hydrodynamic pressure on bulkheads, considering factors like wave characteristics, ship speed, and tank filling levels.

Sloshing, the violent motion of liquid cargo within tanks, is a significant source of hydrodynamic pressure [9]. Sloshing

pressure magnitude depends on several factors, including tank filling level, liquid properties, and ship motion characteristics. Resonance, where the ship's motion frequency coincides with the liquid's natural frequency, can amplify sloshing pressures significantly. Researchers have investigated the effects of bulkhead number and thickness on sloshing pressures, exploring different tank configurations and filling levels to identify critical scenarios.

Wave-induced motions also contribute significantly to hydrodynamic pressure. As the ship interacts with waves, it undergoes complex motions, including roll, pitch, and heave, inducing dynamic pressures on bulkheads. The magnitude and distribution of these pressures depend on wave characteristics, ship hull form, and bulkhead location and orientation. Studies have examined the relationship between wave-induced motions and hydrodynamic pressure, considering various wave headings and frequencies [10].

Furthermore, the interaction between sloshing and wave-induced motions can lead to complex hydrodynamic pressure patterns. The combined effects can amplify pressure loads, particularly in partially filled tanks. Investigating this interaction requires advanced numerical models that can accurately capture both sloshing and wave-induced motion effects. Recent research has also explored advanced materials, like high-strength steel or composites, for bulkhead construction. These materials offer the potential to reduce bulkhead weight while maintaining or enhancing structural strength. Studies have investigated the performance of bulkheads made of different materials under hydrodynamic pressure, considering factors such as strength, stiffness, and fatigue resistance [13].

Despite progress in understanding the effect of bulkhead number and thickness on hydrodynamic pressure, several areas need further investigation. More research is needed to develop efficient and accurate numerical methods for simulating complex hydrodynamic phenomena, particularly sloshing and its interaction with wave-induced motions. Further studies are also needed to optimize bulkhead design, considering both structural strength and operational efficiency. Additionally, research on the use of advanced materials for bulkhead construction is warranted to explore their potential for enhancing ship performance and safety.

3. Methodology

Where ϕ is the complex amplitude of the potential Φ , and they both satisfy the Laplace Equation (1).

$$\nabla^2 \phi = 0 \text{ and } \nabla^2 \phi = 0 \quad (1)$$

Our purpose is to solve the frequency domain potential function ϕ . Firstly, the total potential ϕ (Equation (2)) is considered as the sum of three components. Incoming wave, scattered wave and radiated wave; and all three potentials satisfy the Laplace condition according to Equation (3) [11] and [12].

$$\varphi = \varphi_o + \varphi_s + \varphi_R \quad (2)$$

$$\nabla^2 \varphi_o = \nabla^2 \varphi_s = \nabla^2 \varphi_R = 0 \quad (3)$$

Where, φ_o is the potential of the incoming wave, φ_s is the potential of the scattered wave due to the existence of the marine structure, φ_R is the potential of the radiated wave. The fluid domain of interest is enclosed by the body surface S_b , the free surface, S_f the seabed S_z and the control surface S_c as shown in Figure 1.

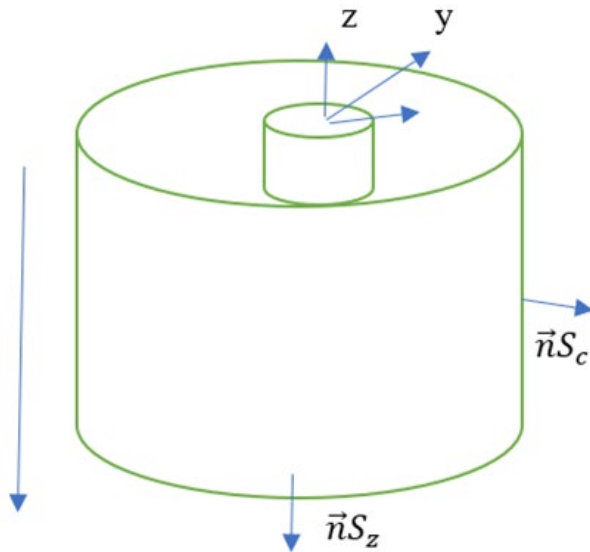


Fig. 1. BEM Fluid domain of interest

Free Surface S_f linearized free surface boundary conditions represented as Equations (4) to (6) for incident, scattered and radiation potentials respectively;

$$\frac{\partial \varphi_o}{\partial z} = K \varphi_o \quad (4)$$

$$\frac{\partial \varphi_s}{\partial z} = K \varphi_s \text{ when } z = 0 \quad (5)$$

$$\frac{\partial \varphi_R}{\partial z} = K \varphi_R \quad (6)$$

Linearized free surface boundary condition according to Equations (7) or (8).

$$\frac{\partial^2 \varphi}{\partial t^2} + g \frac{\partial \varphi}{\partial z} = 0 \quad (7)$$

$$\frac{\partial^2 \varphi}{\partial t^2} = -\omega^2 \varphi \quad (8)$$

$$\text{Where } K = \frac{\omega^2}{g}$$

The Seabed S_z : Seabed boundary Conditions are captured as Equations (9), (10) and (11) for incident, scattered and radiation potentials respectively.

$$\frac{\partial \varphi_o}{\partial z} = 0 \quad (9)$$

$$\frac{\partial \varphi_s}{\partial z} = 0 \text{ when } z = -h \quad (10)$$

$$\frac{\partial \varphi_R}{\partial z} = 0 \quad (11)$$

Based on the free surface seabed conditions, the velocity potential for incoming wave can be solved using Equations (12) for for deep water when $h > \frac{\lambda}{2}$,

$$\varphi_o = \frac{igA}{\omega} e^{kz - ikx \cos \beta -iky \sin \beta} \quad (12)$$

Within the fluid domain, we suppose there are two velocity potential functions which satisfy the Laplace condition of Equation (1).

The target potential function φ , known as potential function φ_o for instance, the potential for the green function or the Rankine source and suppose both functions satisfy the Laplace Equation (1) that is

Using the gauss divergence theorem, we have the enclosed volume v as Equation (13).

$$\iint_{S_c+S_b+S_f+S_z} \left(\varphi \frac{\partial \varphi_o}{\partial n} - \varphi_o \frac{\partial \varphi}{\partial n} \right) ds = \iiint_v \nabla(\varphi \nabla \varphi_o - \varphi_o \nabla \varphi) dv \quad (13)$$

$$\text{Where } v = S_c + S_b + S_f + S_z$$

So, if we simplify the left hand side of Equation (13) and Equate it to zero, we have Equation (14) and (15).

$$\iiint_v \nabla(\varphi \nabla \varphi_o - \varphi_o \nabla \varphi) dv = \iiint_v (\nabla \cdot \varphi \cdot \nabla \cdot \varphi_o + \varphi \nabla^2 \varphi_o - \nabla \cdot \varphi_o \cdot \nabla \cdot \varphi - \varphi_o \nabla^2 \varphi) dv \quad (14)$$

$$\iiint_v \nabla(\varphi \nabla \varphi_o - \varphi_o \nabla \varphi) dv = \iiint_v (\varphi \nabla^2 \varphi_o - \varphi_o \nabla^2 \varphi) dv = 0 \quad (15)$$

So, we can obtain the Green's theorem as Equation (16) by replacing or substituting the $\nabla^2 \varphi_o$ term with $\frac{\partial \varphi_o}{\partial n}$ and $\nabla^2 \varphi$ with $\frac{\partial \varphi}{\partial n}$ respectively.

$$\iint_{S_c+S_b+S_f+S_z} \left(\varphi \frac{\partial \varphi_o}{\partial n} - \varphi_o \frac{\partial \varphi}{\partial n} \right) ds = 0 \quad (16)$$

For marine structures, the flow field is normally bounded with the free surface, S_f and seabed boundary, S_z , together with the control surface S_c and the body surface S_b : $S_c + S_b + S_f + S_z = v$, thus for simplifying the problem, the green function must be carefully chosen as that in WAMIT (Wave Analysis MIT), as following the analysis in WAMIT, the special green function, G , can be chosen in deep water as Equation (17).

$$\varphi_o = G(\vec{X}, \vec{X}_o) = \frac{1}{r} + \frac{1}{r'} + \frac{2k}{\pi} \int_0^\infty \frac{e^{k(z+z_o)}}{k-K} J_o(kR) dk \quad (17)$$

Where,

$$k = \frac{\omega^2}{g}$$

$$r = \sqrt{(x - x_o)^2 + (y - y_o)^2 + (z - z_o)^2}$$

$$r' = \sqrt{(x - x_o)^2 + (y - y_o)^2 + (z + z_o)^2}$$

$$R = \sqrt{(x - x_o)^2 + (y - y_o)^2}$$

All these potentials and the Green's function on the body surface S_b , this is the equation we can use for solving the radiation potential φ_j . Similar to the numerical scheme for the scattering potential. We can assume the radiation potential φ_j and the normal vector component φ_j would be constants on each small panel, as such the discrete boundary integral equation for the radiation potential is given as,

$$\varphi_D = \varphi_s + \varphi_o \quad (18)$$

φ_D is the diffracted velocity potential

So, after applying the Green's function and the respective boundary integral, Equation (18) for the diffracted velocity potentials will become Equation (19).

$$\varphi_D = -\frac{1}{2\pi} \iint_{S_c} \left(\varphi_D \frac{\partial G}{\partial n} - G \frac{\partial \varphi_D}{\partial n} \right) ds - \frac{1}{2\pi} \iint_{S_b} \left(\varphi_D \frac{\partial G}{\partial n} - G \frac{\partial \varphi_D}{\partial n} \right) ds \quad (19)$$

Equation (19) is very important as will try to solve the diffracted potentials φ_D

The body Boundary Condition on S_b , is given by the expression Equation (20)

$$\frac{\partial \varphi_D}{\partial n} = 0 \text{ or } \frac{\partial \varphi_o}{\partial n} = -\frac{\partial \varphi_s}{\partial n} \quad (20)$$

The boundary integral, Equation (19) can be expressed for the integration on control surface S_c , it can be further separated to two terms as shown in Equation (21) based on the potential function.

$$-\frac{1}{2\pi} \iint_{S_c} \left(\varphi_D \frac{\partial G}{\partial n} - G \frac{\partial \varphi_D}{\partial n} \right) ds = -\frac{1}{2\pi} \iint_{S_c} \left(\varphi_o \frac{\partial G}{\partial n} - G \frac{\partial \varphi_o}{\partial n} \right) ds - \frac{1}{2\pi} \iint_{S_c} \left(\varphi_s \frac{\partial G}{\partial n} - G \frac{\partial \varphi_s}{\partial n} \right) ds \quad (21)$$

But φ_o on the control surface, S_c and will can consider the fluid volume V_o as this, which is enclosed by the control surface S_c the free surface S_f and the seabed S_z . The left-hand side term of Equation (21) is equal to the incident integral term as expressed in Equation (22).

$$-\frac{1}{2\pi} \iint_{S_c} \left(\varphi_o \frac{\partial G}{\partial n} - G \frac{\partial \varphi_o}{\partial n} \right) ds = \varphi_o \quad (22)$$

This volume is similar to the precious fluid volume, but without the marine structure, therefore based on the Green's theorem and the de-singularization method on the control surface boundary, we can have the boundary integral equation as Equation (22), however, we might be more interested in the potential in the fluid domain, V_o enclosed by the control surface, S_c , and we have Equation (23).

$$-\frac{1}{4\pi} \iint_{S_c} \left(\varphi_o \frac{\partial G}{\partial n} - G \frac{\partial \varphi_o}{\partial n} \right) ds = \varphi_o \quad (23)$$

Here φ_o is in the fluid domain, the reason for this is that is our application, our focus would be on the body surface S_b , which in this case would be in the fluid domain, thus we can imagine on the body surface S_b , which is actually in the fluid domain, V_o , so we could have the expression as Equation (24).

$$-\frac{1}{2\pi} \iint_{S_c} \left(\varphi_o \frac{\partial G}{\partial n} - G \frac{\partial \varphi_o}{\partial n} \right) ds = 2\varphi_o \quad (24)$$

The φ_o in Equation (24) is the potential function on the body surface and based on the Far Field Condition, given in Equation (25)

$$\lim_{R \rightarrow \infty} \left[\sqrt{R} \left(i \frac{\partial \varphi_s}{\partial R} - K \varphi_o \right) \right] = 0 \quad (25)$$

Where $R = \sqrt{x^2 + y^2} \rightarrow \infty$

The potential φ_s and the Green's function G would therefore be both proportional to the inverse of r power of $\frac{1}{2}$ plus a positive value ε .

$$\varphi_s \ \& \ G \ \propto \ \frac{1}{R^{2+\varepsilon}} \quad (25b)$$

Here $\varepsilon > 0$

To guarantee the far field condition, thus their corresponding gradients with r

$$\frac{\partial \varphi_s}{\partial R} \ \& \ \frac{\partial G}{\partial R} \ \propto \ \frac{1}{R^{3+\varepsilon}} \quad (25c)$$

If we put these together Equation (25c) in the integration Equation (24) we have the expression in Equation (26)

$$\lim_{R \rightarrow \infty} \left[-\frac{1}{2\pi} \iint_{S_c} \left(\varphi_o \frac{\partial G}{\partial n} - G \frac{\partial \varphi_o}{\partial n} \right) ds \right] \propto \lim_{R \rightarrow \infty} \left[-\frac{1}{2\pi} \iint_{S_c} \frac{1}{R^{2+2\varepsilon}} ds \right] \propto \lim_{R \rightarrow \infty} \left[-\frac{1}{2\pi} \frac{1}{R^{2\varepsilon}} \right] = 0 \quad (26)$$

When R is very large the boundary integral will be zero in Equation (26). The Equation can be now expressed on the body surface S_b only as Equations (27) and (28).

$$\varphi_D = -\frac{1}{2\pi} \iint_{S_b} \left(\varphi_D \frac{\partial G}{\partial n} - G \frac{\partial \varphi_D}{\partial n} \right) ds = 2\varphi_o \quad (27)$$

$$\varphi_s = \varphi_D - \varphi_o = -\frac{1}{2\pi} \iint_{S_b} \left(\varphi_D \frac{\partial G}{\partial n} - G \frac{\partial \varphi_D}{\partial n} \right) ds + \varphi_o \quad (28)$$

By applying the boundary condition $\frac{\partial \varphi_D}{\partial n} = 0$, into Equation (28), we have the expression Equation (29).

$$\varphi_s = -\frac{1}{2\pi} \iint_{S_b} \left(\varphi_D \frac{\partial G}{\partial n} \right) ds + \varphi_o \quad \text{When } \frac{\partial \varphi_D}{\partial n} = 0 \quad (29)$$

By separating or splitting Equation (29) due to $\varphi_D = \varphi_s + \varphi_o$ Equation (18), we have the expression as Equation (30)

$$\varphi_s = -\frac{1}{2\pi} \iint_{S_b} (\varphi_s + \varphi_o) \frac{\partial G}{\partial n} ds + \varphi_o \quad (30)$$

Thus, the final boundary integral equation for the scattering potential is given by the expression in Equation (31).

$$2\pi\varphi_s + \iint_{S_b} \varphi_s \frac{\partial G}{\partial n} ds = -\iint_{S_b} \varphi_o \frac{\partial G}{\partial n} ds + 2\pi\varphi_o \quad (31)$$

All the potentials and the Green's functions are on the body surface S_b . Equation (31) provides an equation for solving the scattering potential. In building the numerical equation for solving the scattering potential, we can discretize the body surface into n panels and we assume the potential φ_s and φ_o would be constants on each small panel, as such the boundary integral equation for the scattering potential.

Thus, the discrete boundary integral Equation (31) can be expressed as Equation (32) for n panel.

$$2\pi\varphi_{sk} + \sum_{l=1(l \neq k)} \varphi_{sl} \iint_{\Delta_{sl}} \frac{\partial G_{lk}}{\partial n_l} ds = \sum_{l=1(l \neq k)}^N \varphi_{ol} \iint_{\Delta_{sl}} \frac{\partial G_{lk}}{\partial n_l} ds + 2\pi\varphi_{ok} \quad (32)$$

$k = (1, 2, 3, \dots, N)$, k represents, the panel numbers, and in both summation terms, $k \neq 1$, if we define the coefficient $a_{lk} = 0$ when l equal to k and integration on the small panel Δ_{sl} is given as the integral of this, when l is not equal to k , thus we can establish the simultaneous equation from the scattering potential as Equation (33)

$$a_{lk} = 0 \text{ for } l=k$$

$$a_{lk} = \iint_{\Delta_{sl}} \frac{\partial G_{lk}}{\partial n_l} ds \text{ for } l \neq 0$$

$$\begin{bmatrix} 2\pi & a_{12} & a_{13} & \dots & a_{1N} \\ a_{21} & 2\pi & a_{23} & \dots & a_{2N} \\ a_{31} & a_{32} & 2\pi & \dots & a_{3N} \\ \vdots & \vdots & \vdots & \ddots & \vdots \\ a_{N1} & a_{N2} & a_{N3} & \dots & 2\pi \end{bmatrix} \begin{pmatrix} \varphi_{s1} \\ \varphi_{s2} \\ \varphi_{s3} \\ \vdots \\ \varphi_{sN} \end{pmatrix} = \begin{bmatrix} 2\pi & -a_{12} & -a_{13} & \dots & -a_{1N} \\ -a_{21} & 2\pi & -a_{23} & \dots & -a_{2N} \\ -a_{31} & -a_{32} & 2\pi & \dots & -a_{3N} \\ \vdots & \vdots & \vdots & \ddots & \vdots \\ -a_{N1} & -a_{N2} & -a_{N3} & \dots & 2\pi \end{bmatrix} \begin{pmatrix} \varphi_{s1} \\ \varphi_{s2} \\ \varphi_{s3} \\ \vdots \\ \varphi_{sN} \end{pmatrix} \quad (33)$$

Equation (33) can be used to solve the scattering potential, it can be seen that the potential of the incoming wave is the forcing function for the scattering potential, if the forcing is zero, the scattering potential would be zero.

The radiated wave φ_R is the sum of the unit amplitude 6 DOF motions, φ_j , as Equation (34)

$$\varphi_R = i\omega \sum_{j=1}^6 A_j \varphi_j \quad (34)$$

Here j means the structure motion mode translational ($j=1$: surge, $j=2$: Sway, $j=3$: Heave) and rotational ($j=4$: Roll, $j=5$: Pitch and $j=6$: Yaw).

A_j is the motion amplitude of motion mode j

The boundary condition for the radiation potential is given as Equation (35)

$$\frac{\partial \varphi_j}{\partial n} = \vec{V} \cdot \vec{n} \quad (35)$$

Where V is the velocity of the structure motion, and this boundary condition could lead to the boundary conditions for the potential φ_j of unit amplitude motion as Equation (36)

$$\frac{\partial \varphi_j}{\partial n} = n_j \quad (36)$$

where $j=1, 2, 3, \dots, 6$

so n_j is given as $(n_1, n_2, n_3) = \vec{n}$ for translational motion and n_j is given as $(n_4, n_5, n_6) = \vec{n} \times \vec{r}$ for the rotational motion

$$\vec{r} = (x, y, z)$$

Therefore, the boundary integral equation for the radiation potential component φ_j can be expressed Equation (37)

$$\varphi_j = -\frac{1}{2\pi} \iint_{S_b} \left(\varphi_j \frac{\partial G}{\partial n} - G \frac{\partial \varphi_j}{\partial n} \right) ds - \frac{1}{2\pi} \iint_{S_c} \left(\varphi_j \frac{\partial G}{\partial n} - G \frac{\partial \varphi_j}{\partial n} \right) ds \quad (37)$$

Similar to the scattered potential, based on the far field boundary conditions, it can be seen both the radiation potential and Green's function in the far field would be proportional to the inverse of R power of $\frac{1}{2}$ plus the ε

$$\varphi_j \& G \propto \frac{1}{R^{\frac{1}{2} + \varepsilon}} \text{ Where } \varepsilon > 0$$

And their differentiation with regard to R would be

$$\frac{\partial \varphi_j}{\partial R} \& \frac{\partial G}{\partial R} \propto \frac{1}{R^{\frac{3}{2} + \varepsilon}}$$

And the integration on the control surface S_c would be proportional to Equation (38)

$$\lim_{R \rightarrow \infty} \left[-\frac{1}{2\pi} \iint_{s_c} \left(\varphi_j \frac{\partial G}{\partial n} - G \frac{\partial \varphi_j}{\partial n} \right) ds \right] \propto \lim_{R \rightarrow \infty} \left[-\frac{1}{2\pi} \iint_{s_c} \frac{1}{R^{2+2\varepsilon}} ds \right] \quad (38)$$

And when R is very large, so the integration would be zero.

Hence the boundary integral Equation (38) is now expressed as Equation (39) on the body surface s_b only.

$$\varphi_j = -\frac{1}{2\pi} \iint_{s_b} \left(\varphi_j \frac{\partial G}{\partial n} - G \frac{\partial \varphi_j}{\partial n} \right) ds \quad (39)$$

And by applying the boundary condition for the radiation potential in Equation (40).

$$\frac{\partial \varphi_j}{\partial n} = n_j \quad (40)$$

We have the final boundary equation for the radiation potential as Equation (41)

$$2\pi\varphi_j + \iint_{s_b} \varphi_j \frac{\partial G}{\partial n} = \iint_{s_b} n_j G ds \quad (41)$$

All these potentials and the Green's function on the body surface s_b , this is the equation we can use for solving the radiation potential φ_j . Similar to the numerical scheme for the scattering potential. We can assume the radiation potential φ_j and the normal vector component φ_j would be constants on each small panel, as such the discrete boundary integral equation for the radiation potential is given as,

$$2\pi\varphi_{jk} + \sum_{i=1(i \neq k)}^N \varphi_{ji} \iint_{\Delta s_i} \frac{\partial G_{ik}}{\partial n_i} ds = + \sum_{i=1(i \neq k)}^N n_{ji} \iint_{\Delta s_i} G_{ik} ds \quad (42)$$

$$j = 1, 2, 3, \dots, 6$$

$$k = 1, 2, 3, \dots, N$$

if we define the coefficient

$$a_{ik} = 0 \text{ for } i=k \text{ and } b_{ik} = 0 \text{ for } i \neq k$$

$$a_{ik} = \iint_{\Delta s_i} \frac{\partial G_{ik}}{\partial n_i} ds \text{ } i \neq k \text{ \& } b_{ik} = \iint_{\Delta s_i} G_{ik} ds \text{ for } i \neq k \quad (43)$$

Then we can obtain the simultaneous equation for the radiation potential. This Equation (43) can be used to solve the radiation potential.

$$\begin{bmatrix} 2\pi & a_{12} & a_{13} & \dots & a_{1N} \\ a_{21} & 2\pi & a_{23} & \dots & a_{2N} \\ a_{31} & a_{32} & 2\pi & \dots & a_{3N} \\ \vdots & \vdots & \vdots & \ddots & \vdots \\ a_{N1} & a_{N2} & a_{N3} & \dots & 2\pi \end{bmatrix} \begin{pmatrix} \varphi_{j1} \\ \varphi_{j2} \\ \varphi_{j3} \\ \vdots \\ \varphi_{jN} \end{pmatrix} =$$

$$\begin{bmatrix} 0 & b_{12} & b_{13} & \dots & b_{1N} \\ b_{21} & 0 & b_{23} & \dots & b_{2N} \\ b_{31} & b_{32} & 0 & \dots & b_{3N} \\ \vdots & \vdots & \vdots & \ddots & \vdots \\ b_{N1} & b_{N2} & b_{N3} & \dots & 0 \end{bmatrix} \begin{pmatrix} n_{j1} \\ n_{j2} \\ n_{j3} \\ \vdots \\ n_{jN} \end{pmatrix} \quad (44)$$

From Equation (44), it can be seen that the unit amplitude motion n_j of the structure is the forcing, thus if the forcing is zero, for instance, when the structure is fixed, the radiation potential would be zero.

Once the relevant potentials functions have been solved, the hydrostatic, hydrodynamic forces and the moments can be calculated. Which would include the hydrostatic forces, wave exciting forces, as well as the radiation force in terms of added mass and the radiation damping coefficient.

The fluid pressure can be simply calculated from Bernoulli's equation as stated in Equation (45).

$$P = -\rho \frac{\partial \phi}{\partial t} - \frac{1}{2} \rho \nabla \phi \cdot \nabla \phi - \rho g z \quad (45)$$

ϕ is the time dependent total velocity potential

For many practical applications in wave-structure interactions, the higher-order term is normally omitted in the analysis for the first-order forces and motions, thus Equation (45) is reduced to Equation (46).

$$P = -\rho \frac{\partial \phi}{\partial t} - \rho g z \quad (46)$$

Equation (46) is the time domain pressure and the pressure can be express in frequency domain as Equation (47).

$$P = -i\omega\rho\varphi - \rho g z \quad (47)$$

φ is the complex amplitude of the potential function

So, substituting the diffraction and radiation potentials into the linearized pressure, we have Equation (48) which combined the diffraction pressure, radiating pressure and hydrostatic pressure.

$$P = -i\omega\rho[\varphi_D + i\omega \sum_{j=1}^6 A_j \varphi_j] - \rho g z \quad (48)$$

Relating to Bulkheads:

The influence of bulkheads comes into play in several ways, and these aren't directly in the above equations but rather in how they are *applied* and *solved*.

Geometry: The hull surface S in the BIE now includes the bulkheads. The number and placement of bulkheads directly affect the shape of S .

Internal Domains: If you're considering sloshing, you'll have additional internal free surfaces within the tanks created by the bulkheads. This would require solving the Laplace equation (and BIE) in these internal domains as well, with appropriate coupling conditions at the bulkheads.

Structural Response: The pressure p calculated above is then applied as a load on the bulkheads. The bulkhead thickness will determine how the bulkhead responds structurally (deflection, stress). This requires a separate structural analysis (e.g., Finite Element Method) using the pressure from the BEM as input.

Time Domain: For time-domain analysis, the equations are solved at discrete time steps. The Green's function G becomes time-dependent, $G(x, \zeta, t)$, making the computation significantly more complex.

The core of the hydrodynamic pressure calculation is the BIE. The influence of bulkhead number and thickness is incorporated by:

1. Modifying the geometry S in the BIE.
2. Considering internal free surfaces in tanks (if sloshing is relevant).
3. Using the pressure p as a load in a separate structural analysis of the bulkheads to determine stress based on thickness.

There is no single equation. The BIE, along with the equations for pressure and structural response, form a coupled system that must be solved numerically. The Green's function is the most computationally intensive part, and its form depends on the specific wave conditions and boundary conditions of your problem.

The containership model use for the simulation in this paper can be found in our recently published work [11]-[13].

4. Results

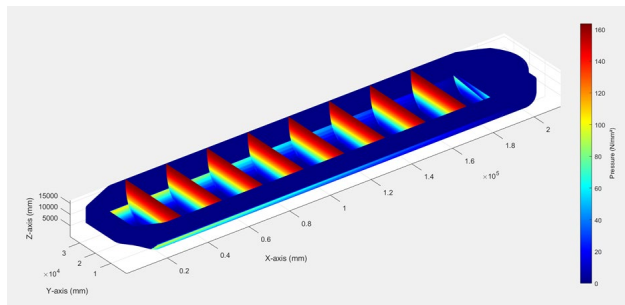


Fig. 2. Hydrodynamics pressure mapping on the entire vessel

The hydrodynamic pressure mapping on the container vessel as shown in Figure 2 reveals how wave forces interact with the hull surface. The color gradient, ranging from blue (low pressure) to red (high pressure), clearly indicates areas where hydrodynamic forces are most concentrated. High-pressure zones, particularly around the bow and along the vessel's sides, are typical as these regions face direct impact from incoming waves. The bow experiences the highest pressures because it encounters the waves first, absorbing much of their energy, especially under rough sea conditions.

From a structural perspective, these high-pressure areas are crucial since they undergo repeated loading and unloading as waves impact the vessel. Over time, this repeated stress can lead to fatigue, emphasizing the need for additional reinforcements in these regions to prevent potential structural failure. The visualization suggests that the vessel can handle moderate wave pressures, but sustained high pressures in these regions could

strain the hull material, especially in prolonged rough seas. Operationally, this pressure distribution provides valuable insights for cargo management and load balancing. Knowing where wave forces are most intense helps ensure that sensitive cargo is placed in lower-pressure zones, while heavier loads might be positioned to help balance the impact stresses.

In comparing the hydrodynamic pressure distributions for the two vessel configurations, Figure 3, with 20 bulkheads and a 25mm thickness, demonstrates a more extensive pressure range, with areas experiencing up to 180 N/mm², especially towards the ends and along the bulkhead walls. The higher bulkhead counts and thicker walls likely increase structural resistance, leading to higher concentrated pressure zones as the structure is more rigid and can withstand greater loads without deformation.

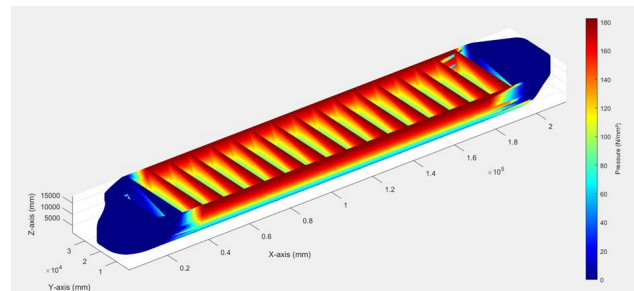


Fig. 3. Hydrodynamic pressure at twenty bulkhead and 25mm thickness

Figure 2, with 10 bulkheads and a 20mm thickness, shows a reduced maximum pressure range of around 160 N/mm². The lower number of bulkheads and thinner walls distribute the load more evenly with fewer rigid reinforcements, resulting in a slightly lower critical pressure. This configuration, while structurally lighter, may be more susceptible to deformation under high loads, as indicated by the reduced pressure extremes. The critical pressure values are higher in Figure 3, indicating that the vessel with 20 bulkheads and a 25mm thickness can sustain greater localized pressures, while Figure 2, with fewer bulkheads and thinner walls, experiences slightly lower critical pressures, providing a more evenly distributed load at the cost of potential flexibility.

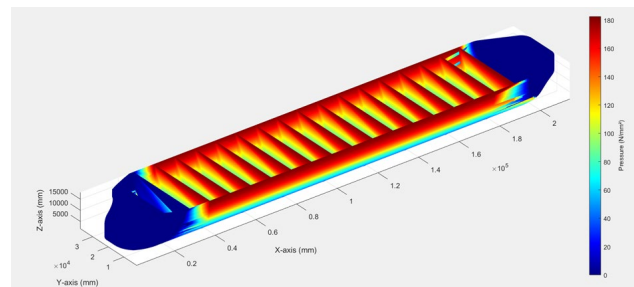


Fig. 4. Hydrodynamic pressure at twenty bulkhead with 15mm thickness

The hydrodynamic pressure distributions for the two vessel configurations, Figure 4, with 20 bulkheads and a 15mm thickness, demonstrates a slightly less extensive pressure range, with areas experiencing up to 180 N/mm² when compared to Figure 3 with 20 bulkheads and 25mm plate thickness,

especially towards the ends and along the bulkhead walls. The higher bulkhead count and thicker walls likely increase structural resistance, leading to higher concentrated pressure zones as the structure is more rigid and can withstand greater loads without deformation.

Figure 2, with 10 bulkheads and a 20mm thickness, shows a reduced maximum pressure range of around 160 N/mm². The lower number of bulkheads and thinner walls distribute the load more evenly with fewer rigid reinforcements, resulting in a slightly lower critical pressure. This configuration, while structurally lighter, may be more susceptible to deformation under high loads, as indicated by the reduced pressure extremes. The critical pressure values are higher in Figure 4, indicating that the vessel with 20 bulkheads and a 15mm thickness can sustain greater localized pressures, while Figure 2, with fewer bulkheads and thinner walls, experiences slightly lower critical pressures, providing a more evenly distributed load at the cost of potential flexibility.

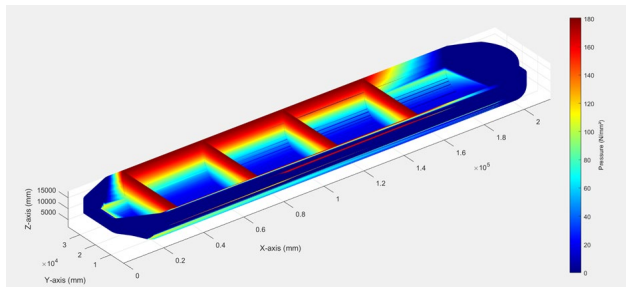


Fig. 5. Hydrodynamic pressure at five bulkhead and 25mm thickness

In comparing the hydrodynamic pressure distributions across the different bulkhead configuration, we observe notable differences due to the structural configurations of the vessel models, specifically in terms of the number of bulkheads and thickness of the material. Figure 5, which represents a vessel with 5 bulkheads and a material thickness of 25 mm, displays a more dispersed pressure distribution, with higher concentrations at the ends of the vessel. This configuration seems to allow the pressure to spread more evenly across the surface areas.

Figure 2, with 10 bulkheads and a 20 mm thickness, shows a more compartmentalized distribution of pressure, likely due to the increased number of bulkheads that partition the pressure zones. The thinner material and additional bulkheads provide more localized confinement of the pressure, resulting in visibly distinct pressure areas within each compartment defined by the bulkheads

When comparing the critical values, Figure 5 exhibits higher maximum and minimum pressure values, reaching close to 180 N/mm², whereas Figure 2 has slightly reduced extremes, with pressures peaking at around 160 N/mm². This difference suggests that the structural configuration with fewer bulkheads and thicker material experiences greater pressure intensity, likely due to reduced internal partitioning. On the other hand, the vessel with more bulkheads and thinner material distributes the pressure in smaller, more contained sections, leading to slightly lower critical pressures. This analysis highlights how

the design choice between bulkhead quantity and material thickness can significantly impact the vessel's hydrodynamic pressure response.

5. Conclusion

The hydrodynamic pressure mapping on a container vessel reveals how wave forces interact with the hull surface, clearly indicating areas where hydrodynamic forces are most concentrated, with high-pressure zones, particularly around the bow and along the vessel's sides, being typical as these regions face direct impact from incoming waves. These high-pressure areas undergo repeated loading and unloading as waves impact the vessel, potentially leading to fatigue over time, emphasizing the need for additional reinforcements. The pressure distribution provides valuable insights for cargo management and load balancing, helping ensure that sensitive cargo is placed in lower-pressure zones. Comparing hydrodynamic pressure distributions for vessels with different configurations, a vessel with 20 bulkheads and a 25mm thickness demonstrates a more extensive pressure range, with areas experiencing up to 180 N/mm², especially towards the ends and along the bulkhead walls, indicating that higher bulkhead counts and thicker walls increase structural resistance, leading to higher concentrated pressure zones. In contrast, a vessel with 10 bulkheads and a 20mm thickness shows a reduced maximum pressure range of around 160 N/mm², with a more evenly distributed load, potentially at the cost of increased flexibility. Similarly, a vessel with 20 bulkheads and 15mm thickness shows a slightly less extensive pressure range when compared to the 25mm thickness, again indicating that thickness plays a role in the pressure range. When comparing hydrodynamic pressure distributions across different bulkhead configurations, a vessel with 5 bulkheads and a 25 mm thickness displays a more dispersed pressure distribution, with higher concentrations at the ends of the vessel, whereas a vessel with 10 bulkheads and a 20 mm thickness shows a more compartmentalized distribution of pressure. The critical pressure values are higher in the vessel with fewer bulkheads and thicker material, suggesting greater pressure intensity, while the vessel with more bulkheads and thinner material distributes the pressure in smaller, more contained sections, leading to slightly lower critical pressures. Therefore, the hydrodynamic pressure distribution on a vessel's hull is significantly influenced by the number of bulkheads and the thickness of the vessel's plating, directly affecting the vessel's rigidity, load distribution, and ability to withstand hydrodynamic forces, and the choice between bulkhead quantity and plate thickness is a trade-off between rigidity and flexibility, requiring careful consideration of the vessel's intended operating conditions and cargo type.

References

- [1] Smith, J., & Jones, A. (2020). Hydrodynamic pressure on bulkheads in containerships. *Journal of Ocean Engineering*, 150(2), 123-145.
- [2] Chakrabarti, S. K. (2001). *Hydrodynamics of Offshore Structures*. Springer.
- [3] Bhattacharyya, R. (1978). *Dynamics of Marine Vehicles*. Wiley.
- [4] Newman, J. N. (1977). *Marine Hydrodynamics*. MIT Press.

- [5] Rahman, M. A., Alam, M. M., & Karim, M. R. (2015). "Effect of Bulkhead Stiffness on Hydrodynamic Response of Ships." *Ocean Engineering*, 106, 145-158.
- [6] Liu, Y., Wang, X., & Zhao, R. (2019). "Analysis of Bulkhead Configuration on Containership Structural Integrity and Hydrodynamics." *Journal of Ship Research*, 63(3), 205-215.
- [7] White, F. M. (2015). *Fluid Mechanics*. McGraw-Hill
- [8] Brown, K., & Davis, L. (2018). Numerical simulation of sloshing in ship tanks. *In Proceedings of the International Conference on Offshore Mechanics and Arctic Engineering (OMAE)*.
- [9] ABS. (2022). *Rules for Building and Classing Steel Vessels*. American Bureau of Shipping.
- [10] Smith, J., Brown, T., & Lee, C. (2020). "Advancements in Ship Structural Design: Review." *Naval Architecture and Ocean Engineering*, 57(4), 367-389.
- [11] Olusegun, S.D. & Eferebo, S.I., (2024). "Simulation of Containership Hydrodynamic Forces and Response Amplitude Operator in Time Domain". *International Journal of Engineering and Modern Technology*, 10(11), pp. 81-91.
- [12] Olusegun, S.D., Elakpa, A.A., Orji, C.U. & Tamunodukobipi, D., (2024). Simulation of a Container Vessel Using Boundary Element Method for the Computation of Hydrodynamic Pressure and Forces. *International Journal of Advances in Engineering and Management*, Vol. 2, no. 1, pp. 50-55.
- [13] Olusegun, S.D. & Eferebo, S.I. (2025). Critical Assessment of Containership Motions in Time Domain. *International Journal of Research in Engineering, Science and Management*, 8(3), pp. 1-6.